Cell Reports
Physical Science

CellPress
OPEN ACCESS

Article

Cationic surfactant for lithium-sulfur batteries enables efficient use of sulfur and limits lithium dendrite formation

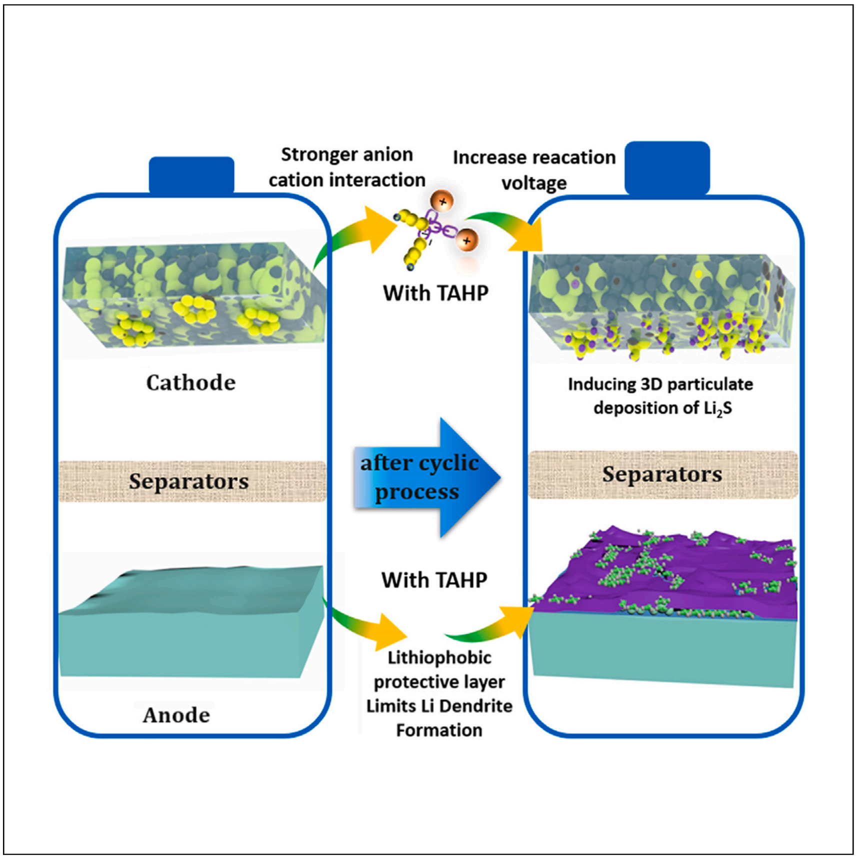

Xiao et al. develop a multi-functional electrolyte additive to enable efficient use of sulfur and limit Li dendrite formation. The strong electrostatic interaction between the cation and the short-chain polysulfide (PS) anion can promote the reduction of long-chain PS to short-chain PS, and the cation lithiophobic protective layer can also suppress the formation of Li dendrites effectively.

Yinglin Xiao, Zhongbo Liu,
Jiachun Wu, ..., Wei Huang,
Guohua Chen, Yonghong Deng

guohchen@cityu.edu.hk (G.C.)
dengyh@sustech.edu.cn (Y.D.)

Highlights

An additive for enhancing LSBs' performance is developed

This additive increases both sulfur utilization and discharge potential

This additive can limit the formation of Li-metal dendrites effectively

Xiao et al., Cell Reports Physical Science 4, 101658
November 15, 2023 © 2023
https://doi.org/10.1016/j.xcrp.2023.101658

Cell Reports
Physical Science

CellPress
OPEN ACCESS

Article

Cationic surfactant for lithium-sulfur batteries enables efficient use of sulfur and limits lithium dendrite formation

Yinglin Xiao,[1,2,9,10] Zhongbo Liu,[3,9] Jiachun Wu,[1] Chang Liu,[1] Yanqiu Peng,[4] Yanchen Fan,[1,5] Jian Chang,[1] Zijian Zheng,[6] Wei Huang,[5,7] Guohua Chen,[8,*] and Yonghong Deng[1,*]

SUMMARY

Lithium-sulfur batteries (LSBs) are promising energy-storage systems due to their high theoretical energy density. However, LSBs' practical energy density is limited by a large electrolyte-to-sulfur (E/S) ratio (>5 μL mg^{-1} S), and their reversible operation encounters challenges from electrode passivation and Li dendrite formation. Herein, we report a strategy for enhancing LSBs' performance by using a cationic surfactant-based electrolyte additive: tetramethylammonium hexafluorophosphate (TAHP). The stronger electrostatic interaction between the tetramethylammonium cation and the short-chain polysulfide (PS) anion promotes the reduction of long-chain PS to short-chain PS, inducing 3D particulate deposition of Li_2S and thus increasing both sulfur utilization and discharge potential, alleviating electrode passivation. Moreover, tetramethylammonium cations can adsorb around Li protrusions to form a lithiophobic protective layer that inhibits the formation of Li dendrites. As a result, the TAHP lithium-sulfur pouch cell maintained an excellent capacity retention ratio with 78.3% after 250 cycles under lean-electrolyte conditions (4.5 μL mg^{-1} sufur [S]).

INTRODUCTION

The ever-growing demand for electric vehicles and portable electronics has increased the need for high-energy-density rechargeable batteries. Among the diversified electrochemical energy storage devices explored, lithium-sulfur batteries (LSBs) are generally accepted as a promising candidate due to their high theoretical specific capacity (1,675 mAh g^{-1}), low toxicity, environmental friendliness, and scalable manufacturing, given the high natural abundance of sulfur.[1–5] However, the practical energy density of LSBs is limited by their large electrolyte-to-sulfur (E/S) ratio (>5 μL mg^{-1} S),[6] high negative-to-positive (N/P) capacity ratio (>5 times excess),[7] and high electrolyte-to-capacity (E/C) ratio (>5 μL mAh^{-1}).[6] Achieving lean-electrolyte-condition reactions (E/S < 5 μL mg^{-1} S) will be critical for enabling the commercial production of high-energy LSBs. However, several major challenges must be overcome for operation in lean-electrolyte conditions: (1) decreased soluble lithium polysulfide (Li_2S_x, $2 < x \leq 8$) dissolution results in sluggish reaction kinetics[7]; (2) the discharge products of Li_2S act as insulators, and their two-dimensional (2D) deposition mode causes electrode passivation, which decreases cycling performance for LSBs[8]; and (3) lower electrolyte quantities facilitate imperfections in the interphase between electrolyte and electrode that enable Li dendrite growth and cause persistent loss of both Li and electrolyte, resulting in fast capacity degradation and even catastrophic safety hazard.[9–13]

[1] Department of Materials Science and Engineering, Guangdong Provincial Key Laboratory of Energy Materials for Electric Power, Southern University of Science and Technology (SUSTech), Shenzhen 518055, China

[2] School of New Energy Science and Engineering, Xinyu University, Xinyu City, Jiangxi Province 338000, P.R. China

[3] Shenzhen Capchem Technology Co., Ltd. Shenzhen, Guangdong province, 518118, P.R. China

[4] EVE Energy Co., Ltd, Huizhou 516006, P.R. China

[5] Petro China Shenzhen Renewable Energy Research Institute Co., Ltd., Shenzhen 518000, P.R. China

[6] Institute of Textile and Clothing (ITC), The Hong Kong Polytechnic University, Hong Kong 999077, P.R. China

[7] National Center for Applied Mathematics Shenzhen (NCAMS, Digital Economy Research Center—De Fin) and College of Business, Southern University of Science and Technology, Shenzhen 518055, P.R. China

[8] School of Energy and Environment City, University of Hong Kong. Tat Chee Avenue, Kowloon, Hong Kong SAR, China

[9] These authors contributed equally

[10] Lead contact

*Correspondence:
guohchen@cityu.edu.hk (G.C.),
dengyh@sustech.edu.cn (Y.D.)

https://doi.org/10.1016/j.xcrp.2023.101658

One effective approach to enable efficient use of sulfur is enhancing the solubility of sulfur redox species and Li_2S and promoting solution-mediated sulfur redox reactions. In this direction, electrolytes with a high Gutmann donor number (DN) can promote sulfur redox reactions and induce 3D particulate deposition of Li_2S, alleviate electrode passivation, and enhance the efficient utilization of sulfur.[14] However, the application of the high DN electrolyte also results in accelerating dendrite formation and low coulombic efficiency. Moreover, high-DN electrolyte decreases the second reduction plateau of LBSs, further compromising the energy density of the LSBs.[15,16]

Herein, we report a new strategy for enhancing LSBs' performance under lean-electrolyte conditions with a new electrolyte additive: tetramethylammonium hexafluorophosphate (TAHP). Our additive encourages high utilization of sulfur and increases the second discharge potential by promoting the electrochemical reduction reaction of long-chain polysulfide (PS) to short-chain PS. TAHP also alleviates electrode passivation by inducing 3D particulate deposition of Li_2S. Moreover, the additive limits the formation of Li-metal dendrites by adsorbing around the Li protrusions to form a lithiophobic protective layer. An optimal additive level (3.75 wt %) of TAHP can greatly enhance the efficient utilization of sulfur under lean-electrolyte conditions (4 μL mg^{-1} S), achieving an initiated capacity of 1,465 mAh g^{-1}, an average coulomb efficiency of 99.4% over 90 cycles, and a sulfur loading of 5.32 mg cm^{-2}.

RESULTS AND DISCUSSION

Cationic surfactant enables efficient use of sulfur

To research the effect of the TAHP electrolyte on LSBs' electrochemical performance under (10 μL mg^{-1} S) E/S ratio conditions, we used the galvanostatic intermittent titration technique (GITT) to measure the equilibrium voltage of the whole discharge and charge plateau. Significantly, the cells with a TAHP electrolyte show higher second discharge plateaus (Figures 1A and 1B). Similar results can be obtained from LSBs cycled under lean-electrolyte conditions (5 μL mg^{-1} S) (Figure S1). As previously reported, the initial stage of the second discharge plateaus (2.1–2.15 V) originates from the electrochemistry reduction reaction of long-chain PS to short-chain $S_4{}^{2-}$ and $S_3{}^{2-}$ PS species.[16–18] Based on this, we hypothesize that TAHP is the main influencing factor on the electrochemistry reduction reactions of long-chain PSs to short-chain $S_4{}^{2-}$ and $S_3{}^{2-}$ species. To prove this, we installed a quartz vessel Li-S cell device to compare the UV-visible (UV-vis) spectroscopy of Li_2S_n and the corresponding digital images of the quartz vessel Li-S cells for both conventional and TAHP electrolytes after discharge to 2.1 V (Figure 1C). The TAHP electrolyte exhibits strong absorption spectrums at 340 and 420 nm (which indicate the presence of $S_3{}^{2-}$ and $S_4{}^{2-}$, respectively) and a weak absorption spectrum at 470 nm (which indicates the presence of the $S_6{}^{2-}$).[19,20] In sharp contrast, the conventional electrolyte shows weak absorption spectrums at 340 and 420 nm and a stronger absorption spectrum at 470 nm. Discharge profiles of quartz vessel lithium-sulfur cell in the conventional electrolyte and the TAHP electrolyte discharged to 2.1 V are shown in Figure 1D. The discharge profiles also show a higher second discharge potential for the TAHP electrolyte, indicating that TAHP can promote the reduction of long-chain $S_6{}^{2-}$ species to short-chain $S_3{}^{2-}$ and $S_4{}^{2-}$ species. The reactions of $S_6{}^{2-}$ to $S_4{}^{2-}$ and $S_3{}^{2-}$ species are shown in Equations 1, 2, and 3.

$$2S_6^{2-} + 2e^- \rightarrow 3S_4^{2-} \quad \text{(Equation 1)}$$

$$S_6^{2-} \rightarrow 2S_3^{\cdot -} \quad \text{(Equation 2)}$$

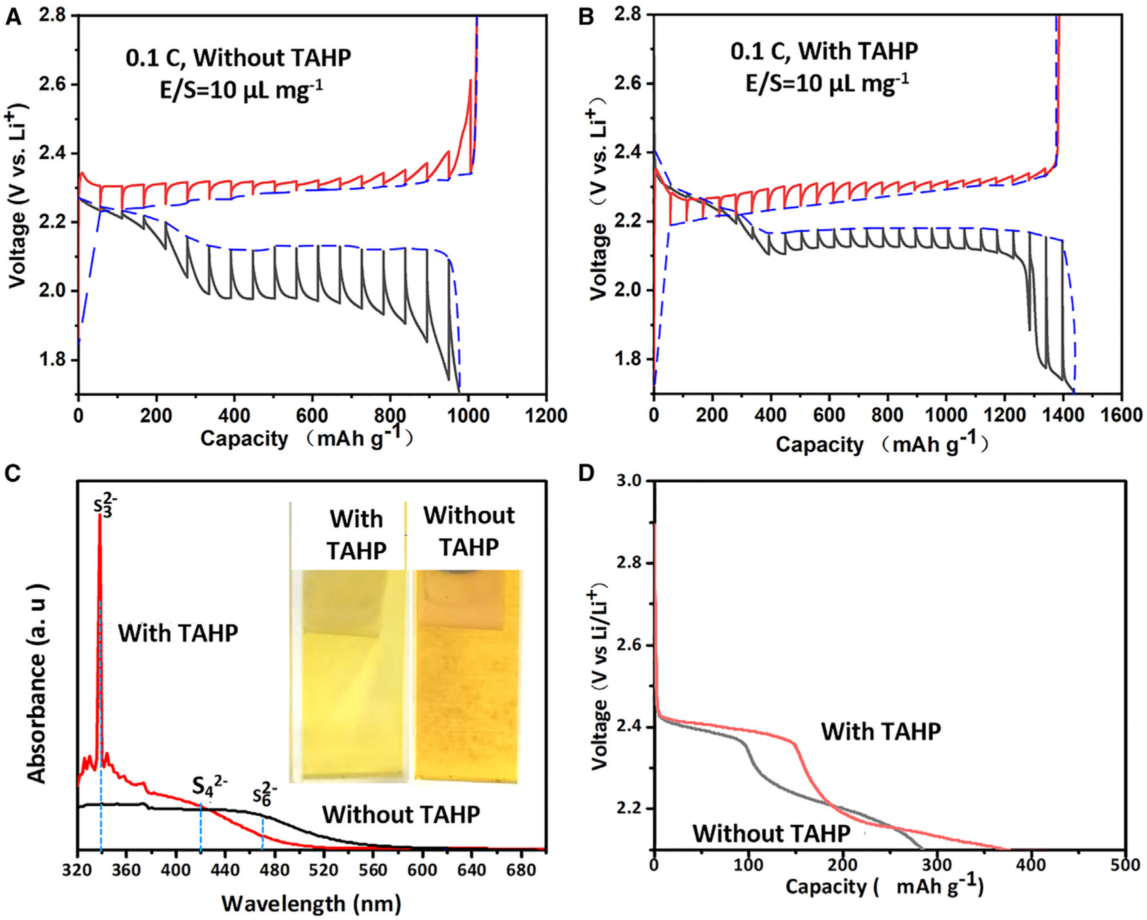

Figure 1. TAHP promotes the electrochemical reduction reaction of long-chain PS to short-chain PS

(A and B) Galvanostatic intermittent titration technique (GITT) results for Li-S half cells in conventional electrolyte (A) and TAHP electrolyte (B). To estimate the voltage curves, quasi-equilibrium potentials from the GITT experiment were connected (dashed lines).

(C) *In situ* UV-vis spectrum and optical coloration images of a quartz vessel lithium-sulfur cell system in conventional (black line) and TAHP (red line) electrolytes, discharged to 2.1 V at a 0.05C current.

(D) Discharge profiles of quartz vessel lithium-sulfur cell in conventional electrolyte and TAHP electrolyte discharged to 2.1 V at current of 0.05C.

$$2S_3^{\cdot -} + 2e^- \rightarrow 2S_3^{2-} \qquad \text{(Equation 3)}$$

The potentials for those reactions are governed by the Nerner equations

$$E_1 = E_0^1 - \frac{RT}{2F}\ln\frac{\alpha^3_{S_4^{2-}}}{\alpha^2_{S_6^{2-}}}, \text{and} \qquad \text{(Equation 4)}$$

$$E_2 = E_0^2 - \frac{RT}{2F}\ln\frac{\alpha^2_{S_3^{2-}}}{\alpha^2_{S_3^{\cdot -}}}, \qquad \text{(Equation 5)}$$

where E_1 and E_2 are the corresponding reduction potential of batteries, $E_0{}^1$ and $E_0{}^2$ are the corresponding standard reduction potentials, F is the Faraday constant (96,485 C mol^{-1}), R is the universal gas constant (8.314 J K^{-1} mol^{-1}), T is the absolute temperature, and α is the chemical activity of the relevant PS species relating to its stabilization.[20,21] Given that $PF_6{}^-$ is not a high-DN salt anion and that there are scarcely any absorption spectrums at 618 nm (which indicates the presence of the $S_3{}^{\cdot -}$) (Figure 1C), this indicates that the $S_3{}^{\cdot -}$ radical is unstable both in the

Table 1. Binding energies of LSB polysulfide anion with Li^+ and $(CH_3)_4N^+$ cations

Polysulfide anion	Binding energy (eV)	
	Li^+	$(CH_3)_4N^+$
S^{2-}	1.732	2.257
S_2^{2-}	1.611	2.491
S_3^{2-}	1.599	2.77
S_4^{2-}	1.923	2.133
S_6^{2-}	2.371	2.395
S_8^{2-}	2.265	2.839

conventional and THAP electrolytes, and the chemical activity of the $S_3^{\bullet-}$ radical in the TAHP electrolyte can be considered equivalent to that of the conventional electrolyte. Therefore, the potentials of the reduction reactions in Equation 5 are determined by the stabilization of the S_3^{2-} species.

To further elucidate the effect of TAHP on the dissolution and stabilization of PS, we employed UV-vis spectroscopy and discovered that the concentration of S_3^{2-} species was higher in the TAHP/DME solution (Figure S2) than in the DME solution. According to a previous report,[19] we attributed TAHP's stabilization of the short-chain S_3^{2-} species to a stronger electrostatic interaction between the $(CH_3)_4N^+$ cations and the short-chain S_3^{2-} anion. To verify this hypothesis, we calculated the binding energies of Li^+ and $(CH_3)_4N^+$ with the PS anion (Table 1). As anticipated, the binding energies of $(CH_3)_4N^+$ with S_4^{2-} and S_3^{2-} are significantly stronger than the binding energies of Li^+ with the PS anion, especially S_3^{2-}. However, we found that the binding energy of $(CH_3)_4N^+$ with S_6^{2-} is almost equal to that of Li^+ with S_6^{2-}, so we theorize that the stronger binding energy of the $(CH_3)_4N^+$ anion with S_4^{2-} and S_3^{2-} may increase the stability and reduce the chemical activity of these PS anions. The nearly equivalent binding energies of $(CH_3)_4N^+$ and Li^+ with S_6^{2-} indicate that $(CH_3)_4N^+$ has little impact on the chemical activity of the S_6^{2-} species, which suggests that the TAHP electrolyte enables a higher reaction voltage in the second discharge plateau, as indicated by Equations 4 and 5. To further evaluate the electrostatic interaction between the $(CH_3)_4N^+$ and Li^+ cations with the S_3^{2-} and S_4^{2-} anion, we calculated their respective solation energies (Table 2) and observed a lower solvation energy for $(CH_3)_4N^+$ in the TAHP electrolyte, indicating a stronger cation-anion electrostatic interaction between $(CH_3)_4N^+$ and S_3^{2-}/S_4^{2-}.[19]

To further explore the interactions between additive, cations, anions, and solvent, molecular dynamics (MD) simulations of 0.5 M S_3^{2-} in electrolytes both containing and not containing TAHP have been performed (Figures 2A–2C). Compared with the conventional electrolyte, more S_3^{2-} were distributed in the interior of the TAHP electrolyte (Figures 2A and 2B) and clustered together with $(CH_3)_4N^+$ cations (Figure 2C), indicating the presence of a stronger cation-anion electrostatic interaction between $(CH_3)_4N^+$ cations and S_3^{2-}. Nuclear magnetic resonance hydrogen spectroscopy (HNMR) of the electrolyte was carried out to investigate the effect of TAHP on the electrolyte (Figure 2D). After adding TAHP, the hydrogen peaks of the conventional electrolyte showed a positive shift, suggesting that PF_6^- anions distributed in the periphery of 1, 3-dioxolame (DOL) and ethylene glycol dimethyl ether (DME), and the formation of F-H bonding resulted in a deshielding effect by showing the positive change of the chemical shift. However, when Li_2S_n was present in the conventional electrolyte, the hydrogen peaks of the conventional electrolyte showed a negative shift. This is due to Li^+ cations distributed in the periphery of DOL and DME molecule, and the formation of O-Li bonding caused a shielding effect,

Table 2. Solvation energies of the cations Li^+ and $(CH_3)_4N^+$

	Solvation energies (kcal/mol)
Li^+	78.73
$(CH_3)_4N^+$	64.35

thus showing the negative change of the chemical shift. After adding TAHP to the conventional electrolyte containing S_n^{2-}, the hydrogen peak of the conventional electrolyte showed a further negative shift, indicating more Li^+ cations shifted to the periphery of the DOL and DME molecules. This may be because the strong interactions between $(CH_3)_4N^+$ cations and S_n^{2-} anions caused S_n^{2-} to move away from the DOL and DME molecules, and thus more Li^+ cations moved around the periphery of these molecules.

To further verify the efficacy of TAHP in lean-electrolyte conditions (4 μL mg^{-1} S), we assembled full LSB cells (both conventional and TAHP) with high sulfur loading. The TAHP LSB cells exhibited more than four times the initiated capacity (1,465 mAh g^{-1} at 0.05C) of the conventional electrolyte LSB cells (326 mAh g^{-1} at 0.05C) (Figure S3). The result authenticates that TAHP can enable efficient utilization of sulfur. The solubility of sulfur redox species is another critical factor for enabling operation of LSBs under lean conditions, so we evaluated the respective dissolution enthalpies (ΔH_{dis}) of the lithium sulfide species (Li_2S_x, x = 1, 3, 4) and the tetramethylammonium sulfide species ($(N(CH_3)_4)_2S_x$, x = 1, 3, 4) (Table 3). Each of the tetramethylammonium sulfide species had much lower dissolution enthalpies than the lithium sulfide species, indicating that the tetramethylammonium sulfide species are more soluble than the lithium sulfide species in TAHP electrolytes and that the tetramethylammonium cation can increase the solubility of sulfur redox species. These results further explain the TAHP electrolyte's fast kinetics for redox reactions, which enables a more efficient utilization of sulfur.[22] We also note that solvents with high PS-anion solubility can induce 3D particulate deposition of short-chain PSs and thus alleviate electrode passivation.[23]

To investigate the growth behavior of short-chain PSs in the conventional electrolyte and the TAHP electrolyte, we used scanning electron microscopy (SEM) to provide the morphologies of the discharging electrode in TAHP and conventional electrolytes after 50 cycles under lean-electrolyte conditions (E/S = 5 μL mg^{-1} S). In the TAHP electrolyte, 3D nanoscale Li_2S particles are deposited on the surface of the electrode (Figure 3A), and the 3D particulate deposition of Li_2S on the surface of the cathode can delayer electrode passivation during discharge. In contrast, in the conventional electrolyte, we observed a 2D-film-like Li_2S deposition morphology (Figure 3E). The insulating 2D deposition Li_2S covered the electrode interfaces, hindering the electrochemical reaction and causing electrode passivation. Such results further corroborate that TAHP can alleviate passivation issue in LSBs. We also employed chronoamperometry (CA) to analyze the electrode passivation. We began by pre-discharging all batteries at 2.15 V for 6 h to eliminate the long-chain LiPSs and recorded the current responses by applying a step potential of 2.05 V. The current signals from the Li_2S electrodeposition show a peaking behavior. Initially, the current decreases because of the Faradaic reaction of the residual long-chain PS[24]; thereafter, the current increases as the Li_2S deposition progresses, peaking at a maximum value. At that point, the nucleation, growth, and overlap of Li_2S passivate the electrode surface, causing a drop in current.[25] In this regime, the maximum current (I_m) and its corresponding time (t_m) can be used to interpret the relative speed of passivation layer formation under different electrolyte systems.

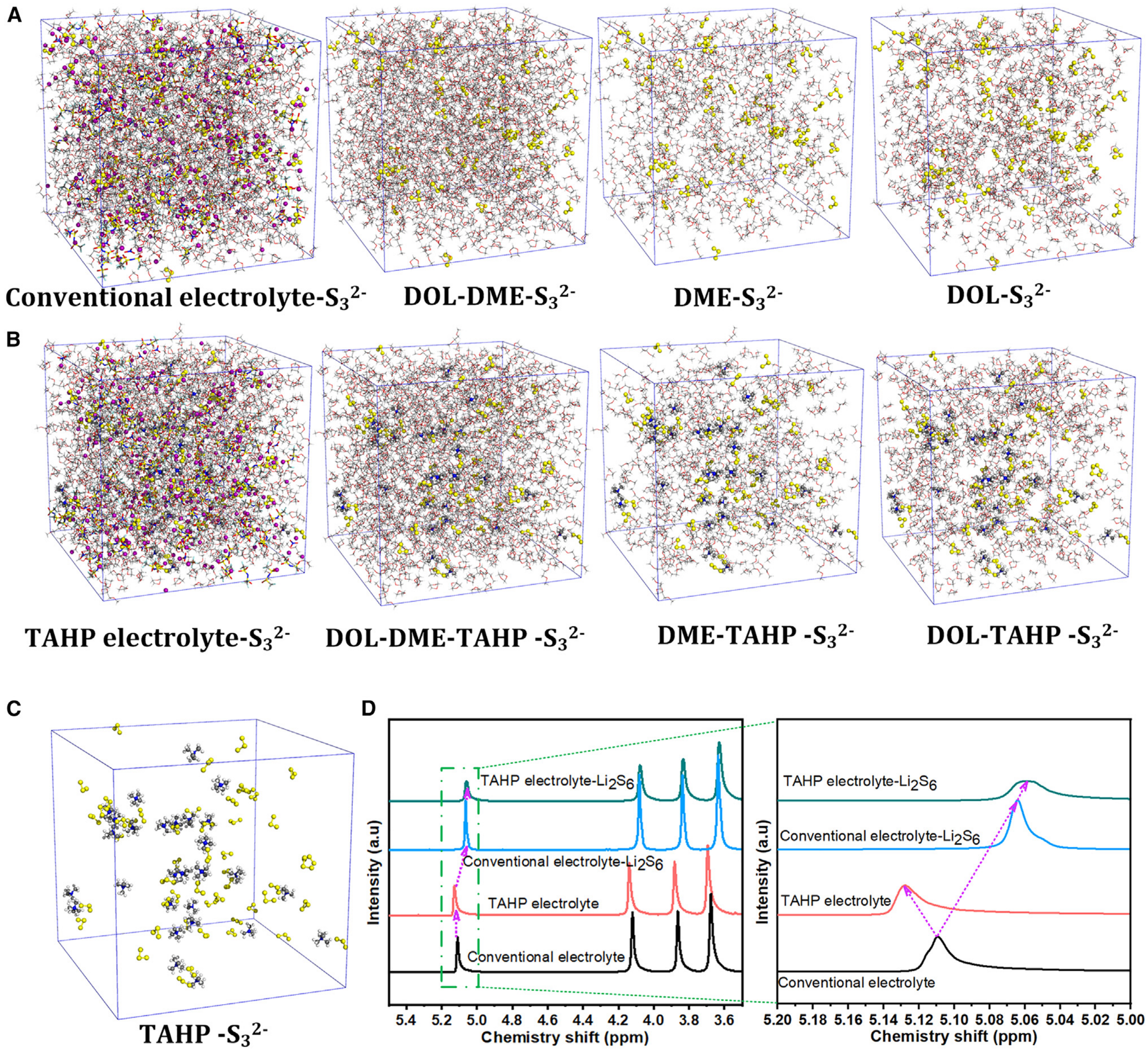

Figure 2. MD simulations investigate the interactions between additive and electrolyte components

(A–C) MD simulate electrolyte structure of S_3^{2-} distributing in electrolytes without TAHP (A) and with TAHP (B and C).

(D) HNMR of conventional electrolyte, THAP electrolyte, conventional electrolyte-Li_2S_6, and THAP electrolyte-Li_2S_6.

Specifically, the duration of the TAHP LSB full cells (t_m: 1,100 s) was more than twice that of the conventional LSBs (t_m: 375 s) (Figures 3B and 3F), indicating that TAHP alleviates the passivation issue in LSBs. To further investigate the deposition behavior of Li_2S varied by TAHP, we obtained similar results via X-ray photoelectron spectroscopy (XPS) of C 1s (Figures 3C and 3G) and S 2p (Figures 3D and 3H). The C 1s peaks at 284. 5 eV correspond to C–C bonds from the carbon host,[8] and C 1s peaks at 286.5 eV and S 2p peaks at 164 eV correspond to C–S bonds binding between host and sulfur. The C–S bonds could be formed through the $S_3^{\bullet-}$ radical to the unsaturated carbon–carbon double bonds of Ketjenblack.[8,24] The sulfur electrode of the conventional electrolyte shows relatively weak C-C (Figures 3C and 3D) and C-S peaks (Figures 3D–3H), suggesting that the carbon host surface was

Table 3. Dissolution enthalpies of tetramethylammonium sulfide and lithium sulfide species

Species	Dissolution enthalpy (kcal/mol)
Li_2S	31.20
$[N(CH_3)_4]_2S$	9.40
Li_2S_3	43.06
$[N(CH_3)_4]_2S_3$	12.63
Li_2S_4	49.41
$[N(CH_3)_4]_2S_4$	3.48

covered by the reaction products after the discharging process, which can deteriorate the interface and cause electrode passivation.[24] The same result is also obtained from XPS of C 1s and S 2p at 200 cycles (Figure S4). This result is also confirmed by electrochemical impedance spectroscopy (EIS) of LSBs in the TAHP electrolyte and the conventional electrolyte (Figure S5). Improved interface impedance in the TAHP electrolyte indicates decreased electrode passivation.

Schematic illustration of TAHP effect on LSBs

Figure 4 summarizes the influences of the $(CH_3)_4N^+$ cations on the electrochemical reaction process of LBSs' and discharge products' deposition morphology (Figure 4A). To evaluate the effect of TAHP on the LSB anode, the lowest unoccupied molecular orbitals (LUMOs) for $(CH_3)_4N^+$, DOL, DME, NO_3^-, PF_6^-, and $TFSI^-$ were calculated by density functional theory (DFT). $(CH_3)_4N^+$ showed the lowest LUMO energy level (Figure 4B), suggesting that $(CH_3)_4N^+$ reduction would occur at a potential higher than the other electrolyte components. This is confirmed by the cyclic voltammetry (CV) measurements of the TAHP electrolyte and the conventional electrolyte on stainless-steel electrodes (Figure S6). Considering its azote-containing structure of $(CH_3)_4N^+$, one would expect abundant Li_3N content in the solid-electrolyte interphase (SEI) on the lithium electrodes. XPS was performed on Li-metal electrodes recovered from LSBs after 200 cycles, which provide information regarding surface element species (Figure S7). Compared with the conventional electrolyte, the TAHP electrolyte exhibits stronger absorption spectrums at 65 eV nm corresponding to the C–Li bond originating from Li_3N. Earlier research indicated that Li_3N was beneficial to form uniform, mechanically durable, electrochemically stable, high-flexibility interphases, which can suppress Li dendrite growth effectively. Moreover, lithium nitrate was used as an electrolyte additive to improve the electrochemical performance of LSBs by forming an inorganic-rich SEI on the surface of the Li anode that suppresses Li dendrite growth.[26–28] The combined action of $(CH_3)_4N^+$ and NO_3^- would cause the SEI to have more stability. However, the large volume expansion of the Li anode during the discharging-charging process could cause the SEI to crack or break, allowing Li dendrites to protrude into/across the SEI.[29,30] In contrast, with the TAHP electrolyte, if the SEI cracks/breaks, the undecomposed $(CH_3)_4N^+$ ions adsorb around nascent Li protrusions, forming a lithiophobic protective layer under the action of electric field force and surface tension. This lithiophobic protective layer drives the Li^+ away from Li protrusion regions, minimizing dendrite formation.[31,32] In addition, TAHP can effectively suppress Li dendrite growth; a schematic of the synergistic effect of TAHP and $LiNO_3$ on suppressing Li dendrite growth is shown in Figure 4C.

Cationic surfactant limits Li dendrite formation

To evaluate the stability of the Li metal in TAHP LSBs and to optimize the quantity of TAHP for LSB performance, we performed Li-Cu cell tests with different TAHP ratios (2.50, 3.75, and 5.00 wt %) at a current density of 1 mA cm^{-2} and a deposition

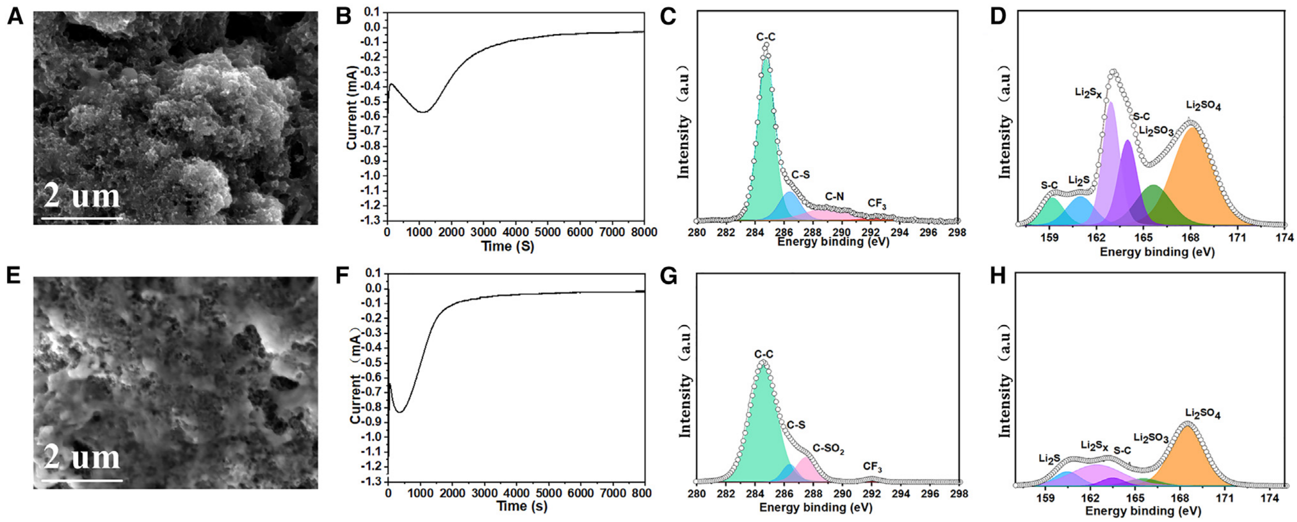

Figure 3. TAHP alleviates electrode passivation

(A and E) SEM images of the fully discharged cathodes after 50 cycles for the TAHP electrolyte (A) and conventional electrolyte (E).

(B and F) CA of the TAHP electrolyte (B) and conventional electrolyte (F).

(C, D, G, and H) XPS analysis of C 1s (C, G) and S 2p (D, H) spectra of the TAHP cathodes (C and D) and conventional cathodes (G and H) after 50 cycles at charge state.

capacity of 1 mAh cm^{-2}. Our results suggest that 3.75 wt % TAHP enabled the best LSB performance (Figure S8), so we used 3.75 wt % TAHP to investigate the electrochemical performance of the TAHP LSB. The resulting coulombic efficiency (CE) tests of Li-metal plating/stripping in the TAHP and conventional electrolytes were performed at two current densities: 0.5 and 1 mA cm^{-2}. The conventional Li-Cu cell failed within 390 cycles at a current density of 0.5 mA cm^{-2} with a fixed capacity of 0.5 mAh cm^{-2}; in sharp contrast, the TAHP Li-Cu cell survived 780 cycles of constant current cycling without failing under the same conditions (Figure 5A). At the higher current of 1 mA cm^{-2} with a fixed capacity of 1 mA cm^{-2}, the conventional Li-Cu cell failed at 160 cycles, while the TAHP Li-Cu cell was still performing after 380 cycles (Figure 5B). The results clearly demonstrate that TAHP is critical to the stabilization of the Li-metal anode.

To further evaluate the effects of TAHP on the anode, we assembled Li-Li symmetrical cells and compared the voltage profiles of the TAHP and conventional electrolytes at a galvanostatic of 1 mA cm^{-2} with deposition capacities of 1 (Figure 5C) and 4 mAh cm^{-2} (Figure 5D). In TAHP electrolytes, the overpotential of Li plating/stripping remained stable when the cell was polarized at 1 mA cm^{-2} with a deposition capacity of 1 mAh cm^{-2} for 2,000 h. In sharp contrast, the overpotential of the conventional electrolyte aggravated monotonously after 900 h. When the deposition capacity is increased to 4 mAh cm^{-2}, the overpotential of Li plating/stripping that remains is also far more stable for the TAHP electrolyte (780 h) than for the conventional electrolyte (225 h). To better explain this discrepancy, we took EIS measurements to illustrate the kinetics of the Li anode (Figure S9) and discovered that the interface resistance of the TAHP electrolyte is slightly higher than that of the conventional electrolyte after 1 cycle, probably due to the adsorption of surfactant molecules on the surface of the Li anode, which acts as a physical barrier that hinders Li$^+$ transport.[33] Nevertheless, after 50 cycles, the interface resistance for TAHP Li-Li symmetrical cells is much smaller than that of conventional Li-Li symmetrical cells due to the stable solid-liquid interface created by TAHP.[33] Similar results were

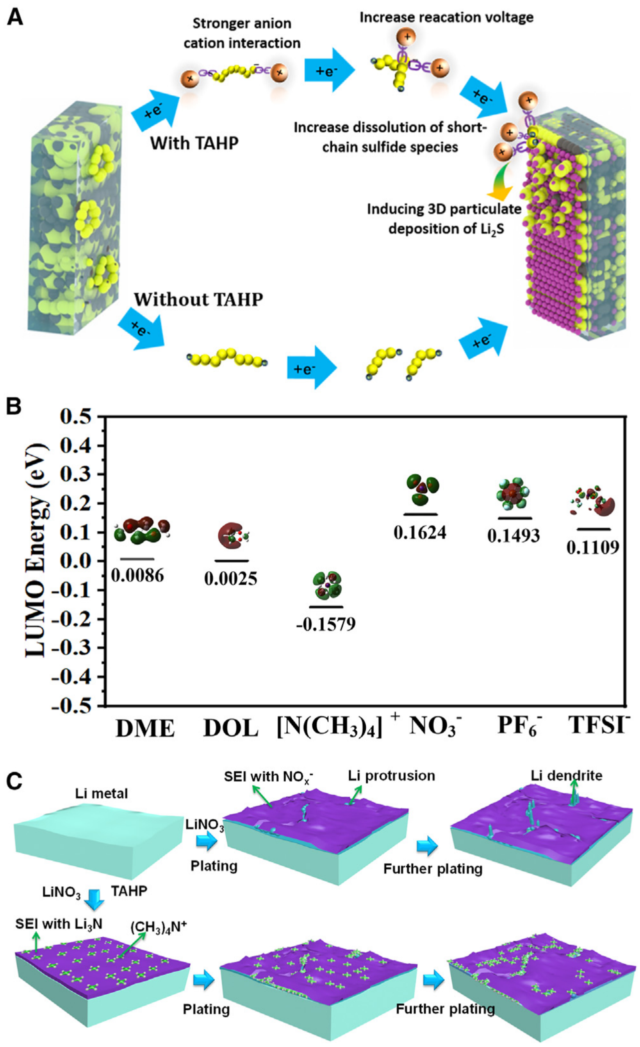

Figure 4. Schematic illustration of TAHP effect on the electrochemical reaction process and cathode and anode interfaces

(A) TAHP promotes the reduction of long-chain SPs to short-chain SPs and induces 3D particulate deposition of discharge products.

(B) LUMO energies of $(CH_3)_4N^+$, DOL, DME, NO_3^-, PF_6^-, and $TFSI^-$.

(C) Synergistic effect of TAHP and $LiNO_3$ on suppressing Li dendrite growth.

obtained from the plating/stripping profiles for Li-Cu cells in the TAHP electrolyte and the conventional electrolyte (Figure S10). SEM images of the Li metal from Li-Li symmetrical cells show that, after cycling with TAHP, the Li-metal surface appears smooth and dense after 10 (Figure 5E), 50 (Figures 5F and 5G), and 750 cycles (Figure S11), with no dendrite formation. After similar cycling with the conventional electrolyte, Li protrusions are clearly visible on the surface of the Li electrode after only 10 cycles (Figure 5H), with obvious dendritic whiskers visible after 50 cycles (Figures 5I and 5J). We obtained similar results by imaging the surface of the Li electrode from TAHP and conventional LSBs (Figure S12) and by taking *in situ* optical photographs of Li-Cu cells with TAHP (Figure 5K) and conventional (Figure 5L) electrolytes during the lithium-plating processes. The video of *in situ* Li-Cu cells with the TAHP electrolyte shows no growth of the lithium dendrite during the whole plating lithium process (Video S1). In contrast, lithium dendrite with the conventional

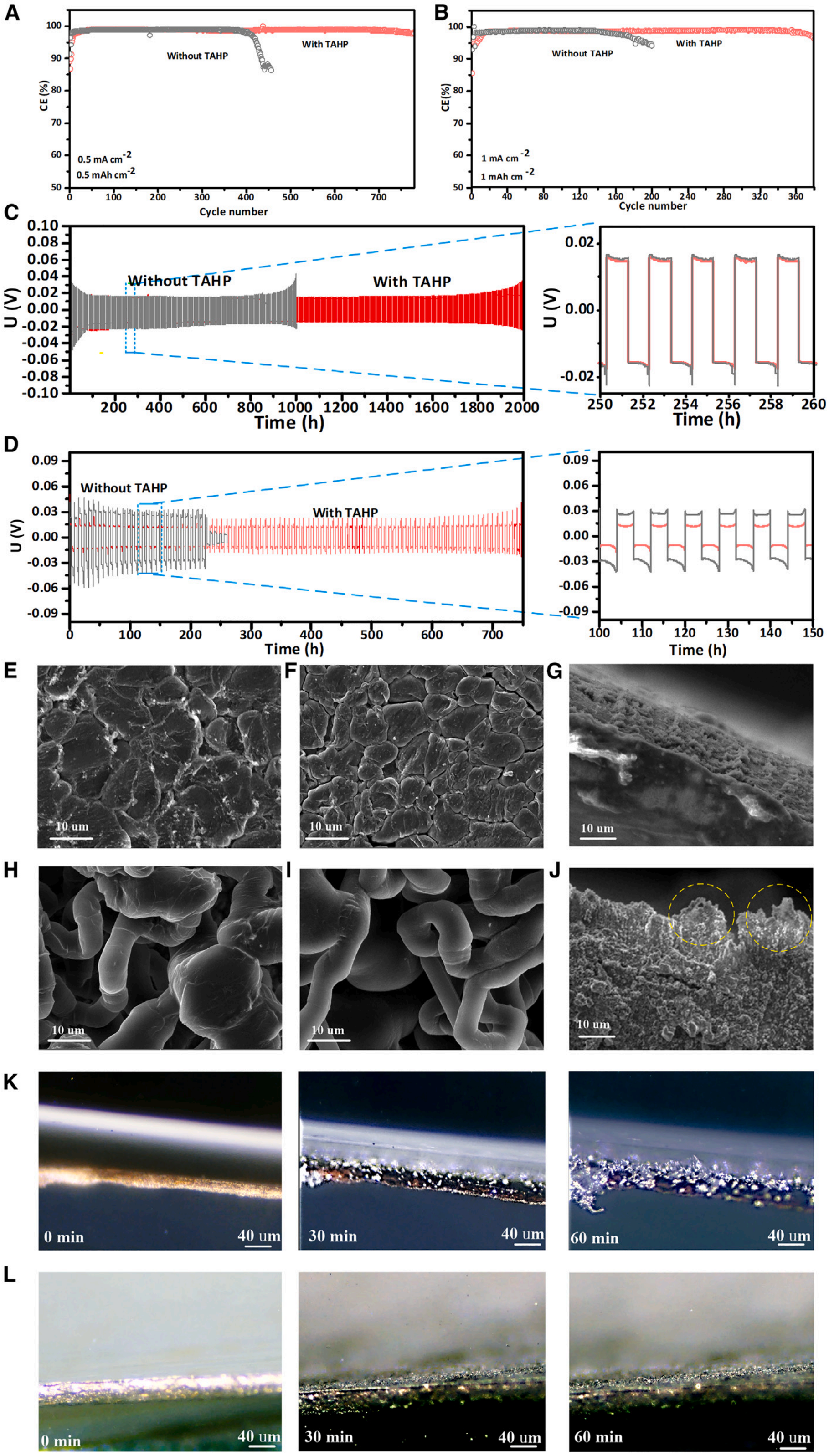
A
CE (%)
Cycle number
Without TAHP
With TAHP
0.5 mA cm^{-2}
0.5 mAh cm^{-2}
B
CE(%)
Cycle number
Without TAHP
With TAHP
1 mA cm^{-2}
1 mAh cm^{-2}
C
U (V)
Time (h)
Without TAHP
With TAHP
D
U (V)
Time (h)
Without TAHP
With TAHP
E
F
G
H
I
J
10 um
K
0 min
30 min
60 min
40 um
L
0 min
30 min
60 min
40 um

Figure 5. TAHP limits the formation of Li-metal dendrites

(A and B) CE tests of Li-Cu cells at current densities of 0.5 (A) and 1 mA cm^{-2} (B) in TAHP and conventional electrolytes.

(C and D) The voltage profiles of Li-Li cell during Li plating/stripping at a current density of 1 mA cm^{-2} and fixed capacities of 1 (C) and 4 mAh cm^{-2} (D) in TAHP and conventional electrolytes (C and D).

(E–J) SEM of symmetric Li-Li cells after 10 cycles (E and H) and 50 cycles (F, G, I, and J) using TAHP electrolyte (E–G) and conventional electrolyte (H–J).

(K and L) *In situ* digital photographs of Li-Cu batteries in conventional electrolyte (K) and TAHP electrolyte (L) during the lithium-plating process. The digital photographs of (K) and (L) originate from Videos S1 and S2, respectively.

electrolyte is formed gradually at the same conditions (Video S2). Again, the TAHP electrolyte images show thin, uniform Li particle deposition, while the conventional electrolyte images show Li whiskers on the Cu surface within 30 min and significant whisker growth after 60 min. Collectively, these characterizations confirm that TAHP effectively suppresses the formation of Li dendrites in LSBs.

Effect of the TAHP electrolyte on electrochemical performance of LSBs

To test the stabilization of the Li-metal anode and the efficient utilization of sulfur in LSBs, we constructed full cells with high sulfur loading (Li-metal anode in 10% excess of the sulfur cathode). The TAHP LSBs dramatically outperformed the conventional LSBs at 0.05 C (1C = 1,675 mA g^{-1}) (Figures 6A–6D) and 0.1C (Figures 6E and 6F) under lean-electrolyte conditions. With a sulfur loading of 5.32 mg cm^{-2}, the TAHP LSBs achieved an initial capacity of 1,465 mAh g^{-2}, fading to 560 mAh cm^{-2} after 90 cycles, with an average 99.4% CE under lean-electrolyte conditions (4 μL mg^{-1} S). Even under sparse electrolyte conditions (3 μL mg^{-1} S), with a sulfur loading of 4.4 mg cm^{-2}, the TAHP LSB achieved an initial capacity of 1,375 mAh g^{-1}, fading to 560 mAh g^{-2} after 140 cycles (42% retention) with an average 98.7% CE. Compared with previous reports, this work shows a lowest E/C ratio at 0.1C (Table S1), indicating that TAHP has significant potential for application in LSBs. Under both conditions, the TAHP LSB radically outperforms conventional LSBs, which fail almost immediately under both lean-electrolyte conditions (initial capacity of 326 mAh g^{-1}, sulfur loading of 5.14 mg cm^{-2}) (Figures 6C–6F) and sparse-electrolyte conditions (initial capacity of 1.51 mAh g^{-1}) (Figures 6A and 6B).

To demonstrate the broad utility of TAHP, we also obtained similar results by testing half cells under lean-electrolyte conditions (Figure S13), where the TAHP LSBs show significant improvement for capacities and cycling stability at 0.05C, 0.1C, and 0.5C. We further verified these trends by measuring and comparing the cycling performances of TAHP and conventional LSB full cells (Figure S14) under excessive-electrolyte conditions (15 μL mg^{-1}); even then, TAHP improved the stabilization of the Li-metal anode and enabled efficient sulfur utilization.

To further evaluate the effects of TAHP on extreme-condition LSBs, we assembled pouch cells with high sulfur loading (5.31 mg cm^{-2}) and a Li-metal anode in 200% excess of the sulfur cathode (Figure 6G). Compared with the conventional LSB full cells, the TAHP LSB pouch cells show improved cycling stability, with an initial charging capacity of 217 mAh, a charging capacity of 170 mAh after 250 cycles (78.3% retention), and a higher median voltage (Figure S15) under lean-electrolyte conditions (4.5 μL mg^{-1} S). Even TAHP LSB pouch cells show excellent electrochemistry performance under lean-electrolyte conditions of 3.5 μL mg^{-1} S (Figure 6H). We also assembled a larger-capacity TAHP LSB full cell (~3 Ah) and carried out cycling performance tests at 15°C for 30 cycles and 30°C for 80 cycles (Figure S16). The TAHP LSB showed outstanding applicability at low temperature and excellent cycling performance at room temperature.

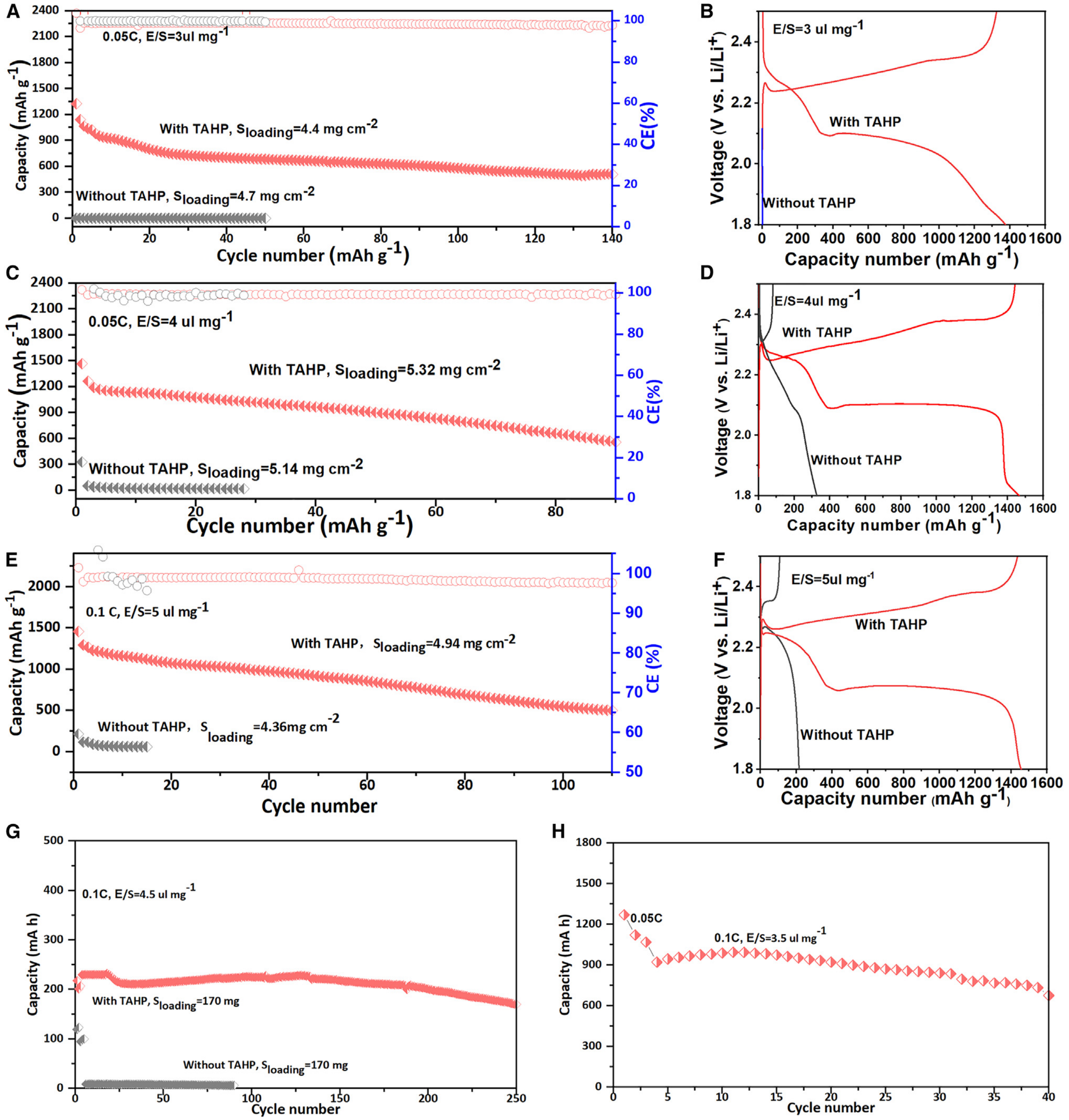

Figure 6. TAHP improves LBSs' electrochemistry performance

(A–F) Full cell cycling performance and corresponding initial discharge/charge profiles of LSBs with TAHP (red) and conventional (gray) electrolytes under lean-electrolyte conditions at 0.05 C (A–D) and 0.1 C (E and F).

(G) Pouch cell cycling performance of LBSs in conventional electrolyte and TAHP electrolyte under electrolyte condition of 4.5 µL mg^{-1} S at 0.1 C.

(H) Pouch cell cycling performance of LBSs in TAHP electrolyte under electrolyte condition of 3.5 µL mg^{-1} S at 0.1 C.

In summary, LSBs' practical application is limited by large electrolyte usage, Li dendrite formation, and electrode passivation. Herein, we report the performance of an electrolyte additive: TAHP for LSBs. The TAHP LSBs consistently outperform conventional electrolyte LSBs via three mechanisms: (1) by promoting the reduction of long-chain PS to short-chain PS, TAHP enables high discharge potential and the high utilization of sulfur under lean-electrolyte conditions; (2) by inducing 3D particulate deposition of Li_2S, TAHP alleviates electrode passivation; and (3) because TAHP's $(CH_3)_4N^+$ ions adsorb around the Li protrusions, they form a lithiophobic protective layer that completely suppresses the formation of Li dendrites. TAHP LSB pouch cells with high sulfur loading (170 mg) show improved cycling stability, with an initial charging capacity of 217 mAh and a charging capacity of 170 mAh after 250 cycles (78.3% retention) under lean-electrolyte conditions (4.5 $\mu L\ mg^{-1}$ S). In a much broader context, this new additive also shows significant potential for application in alkali metal-sulfur batteries or any batteries that employ Li-metal anodes.

EXPERIMENTAL PROCEDURES

Resource availability

Lead contact

Further information and requests for resources and materials should be directed to and will be fulfilled by the lead contact, Yinglin Xiao (xylin2015@126.com).

Materials availability

The study did not generate new unique reagents.

Data and code availability

The authors declare that the data used are available upon request from the lead contact and in the supplemental information.

Material and electrode preparation

The C/S composite and working electrodes were prepared according to the previous method.[34] The half cells were assembled with sulfur loading of 0.7–3 mg cm^{-2} on an aluminum (Al) foil collector and an electrolyte/sulfur ratio of 3–15 $\mu L\ mg^{-1}$ S. 3D current collector electrodes were prepared according to the previous method,[34] with sulfur loading of 4–6 mg cm^{-2} with an electrolyte/sulfur ratio of 3–5 $\mu L\ mg^{-1}$ and a low N/P capacity ratio (<1.2 times excess).

Preparation of electrolytes

The base electrolyte with 1.0 M LiTFSI and 4 wt % $LiNO_3$ in DOL and DME (1:1 by volume) was purchased from Suzhou Duoduo Chemical Technology. TAHP was purchased from J&K Scientific. The TAHP electrolyte was prepared by dissolving different ratios of TAHP (2.50, 3.75, and 5.00 wt %) in conventional electrolyte.

Electrochemical testing

Full battery and half battery cycling performance tests were carried out on a Neware battery tester in the voltage window of 1.8–2.5 or 1.7–2.6 V versus Li^+/Li, respectively, and all tests were performed at 30°C. For the CA measurements, cells were pre-discharged at 2.15 V for 6 h to reduce the long-chain PS anion. After that, the current responses were recorded by applying a static potential of 2.05 V. EIS spectra were collected using a PARSTAT4000A (Princeton Applied Research, Oak Ridge, TN, USA) electrochemical workstation in the frequency range of 1 MHz–100 Hz with an alternating spectrum (ac) perturbation of 10 m at open circuit potential. CV measurements of conventional and TAHP electrolytes were carried out on a PARSTAT4000A electrochemical workstation using stainless-steel electrodes at a scan speed of 5 mV s^{-1} to confirm the electrochemical stability window of TAHP. GITT tests were carried out on a Neware battery tester between 1.7 and 2.8 V versus Li^+/Li, using Li-S half cells with sulfur loading of 1.0–1.5 mg cm^{-2}. The GITT experiments consist of a series of pulse currents at 0.1C for 20 min, each followed by a

120 min open circuit period. A galvanostatic Li plating/stripping test was conducted using a lithium-copper (Li-Cu) cell and a symmetric lithium-lithium (Li-Li) cell. For the lithium-copper cell, a commercial Cu current collector was cut into a disk (Φ18 mm). A lithium metal foil (Φ16 mm) and a Celgard 2400 PP membrane (Φ19 mm) were used as a negative electrode and a separator, respectively, and a 40 μL electrolyte was assembled. The cells were cycled from 0 to 1.0 V with current densities of 0.5 and 1 mA cm^{-2} and fixed capacities of 0.5 and 1 mAh cm^{-2}, respectively. For the symmetric lithium-lithium (Li-Li) cell, the cell was assembled with 40 μL electrolyte, and we used lithium metal foils (Φ14 mm) as negative electrodes, Celgard 2400 PP membranes (Φ19 mm) as separators, and Cu foil (Φ18 mm) as the counter electrode. The symmetric lithium-lithium cells were first discharged to deposit Li metal with capacity of 10 mAh cm^{-2} on Cu foil at a current density of 0.1 mA cm^{-2}. After that, the cells were cycled and fixed at capacities of 1 and 4 mAh cm^{-2} at a current density of 1 mA cm^{-2}.

Li_2S_6 dissolution experiment

S and Li_2S with a mole ratio of 5:1 (32 and 9.2 mg) were added into 10 mL DME solvent. After that, samples stood for 48 h under 60°C temperature. Then, the prepared solution was diluted to 2 mM, and 3.75 wt % TAHP was added into the solution as a contrast sample. Finally, UV-vis spectroscopy of the diluted Li_2S_6 in the DME solution and the TAHP solution was measured on a UV-vis spectrophotometer (Lambda 750s).

In situ cell testing

The *in situ* cell was assembled in a micro-quartz cuvette with 2 mL volume; a copper foil or sulfur electrode was used as the cathode electrode, and Li metal was used as the anode. Celgard 2500 (Hefei Kejing Materials Technology) was used to insulate the cathode from the anode. The electrolyte with the same volume was injected to the micro-quartz cuvette for *in situ* cell testing. The pouch cell was provided by Shenzhen Qichen New Energy Technology. The digital photographs of the whole quartz vessel Li-S cell system and pouch Li-S cell are provided in Figure S17.

Characterizations

SEM studies of electrode morphologies were performed on a scanning electron microscope (JSM-6360). The surface chemistry of electrodes were collected by an XPS system (Thermo Scientific, Waltham, MA, USA). HNMR of the electrolyte was carried out on an NMR spectrometer (Bruker Avance III HD 400MHz). For further information, see the supplemental experimental procedures.

SUPPLEMENTAL INFORMATION

Supplemental information can be found online at https://doi.org/10.1016/j.xcrp.2023.101658.

ACKNOWLEDGMENTS

The authors gratefully acknowledge funding support from the Key Area Research and Development Program of Guangdong Province (2019B090908001), the Science and Technology Planning Project of Guangdong Province (2020A0505090011), and Shenzhen Key Projects (JCYJ 20220818100218040), and Guangdong Provincial Key Laboratory of Energy Materials for Electric Power (2018B030322001).

AUTHOR CONTRIBUTIONS

Y.D. conceived and supervised the project. Y.X. conducted electrolytes, materials, and electrode preparation, electrochemical testing, and the characterizations of SEM and XPS spectra of cathodes after 50 cycles; designed electrolyte additives and experiments; and wrote the paper. G.C. provided the cathode electrodes and LSBs pouch cells and participated in result & discussion. Z.L. designed electrolyte formula and studied the electrolytes/electrodes interface. J.W. conducted NMR spectrometer testing, the characterizations of XPS spectra of electrodes after 200 cycles, and electrochemical stability window of electrolyte testing. C.L. conducted Li_2S_6 dissolution experiment and UV-VIS spectrophotometer testing. Y.F. conducted the calculation of binding energies of polysulfide anions with Li^+ and $(CH_3)_4N^+$ cations. Y.P., J.C., Z.Z., and W.H. participated in the discussion and the interpretation of the various results.

DECLARATION OF INTERESTS

The authors declare no competing interests.

Received: February 10, 2023
Revised: July 22, 2023
Accepted: October 3, 2023
Published: November 15, 2023

REFERENCES

1. Dörfler, S., Althues, H., Härtel, P., Abendroth, T., Schumm, B., and Kaskel, S. (2020). Challenges and Key Parameters of Lithium-sulfur batteries on pouch cell level. Joule *4*, 539–554.
2. Fan, L., Li, M., Li, X., Xiao, W., Chen, Z., and Lu, J. (2019). Interlayer material selection for lithium-sulfur batteries. Joule *3*, 361–386.
3. Zhou, J., Liu, X., Zhu, L., Zhou, J., Guan, Y., Chen, L., Niu, S., Cai, J., Sun, D., Zhu, Y., et al. (2018). Deciphering the modulation essence of p Bands in Co-based compounds on Li-S chemistry. Joule *2*, 2681–2693.
4. Pang, Q., Shyamsunder, A., Narayanan, B., Kwok, C.Y., Curtiss, L.A., and Nazar, L.F. (2018). Tuning the electrolyte network structure to invoke quasi-solid state sulfur conversion and suppress lithium dendrite formation in Li-S batteries. Nat. Energy *3*, 783–791.
5. Tian, H., Tian, H., Wang, S., Chen, S., Zhang, F., Song, L., Liu, H., Liu, J., and Wang, G. (2020). High-power lithium-selenium batteries enabled by atomic cobalt electrocatalyst in hollow carbon cathode. Nat. Commun. *11*, 5025.
6. Bhargav, A., He, J., Gupta, A., and Manthiram. (2020). A. A Lithium-Sulfur Batteries: Attaining the Critical Metrics. Joule *4*, 278–291.
7. Cheng, L., Curtiss, L.A., Zavadil, K.R., Gewirth, A.A., Shao, Y., and Gallagher, K.G. (2016). Sparingly Solvating Electrolytes for High Energy Density Lithium−Sulfur Batteries. ACS Energy Lett. *1*, 503–509.
8. Pan, H., Han, K.S., Engelhard, M.H., Cao, R., Chen, J., Zhang, J.G., Mueller, K.T., Shao, Y., and Liu, J. (2018). Addressing passivation in lithium-sulfur battery under lean electrolyte condition. Adv. Funct. Mater. *28*, 1707234.
9. Li, G., Huang, Q., He, X., Gao, Y., Wang, D., Kim, S.H., and Wang, D. (2018). Self-formed hybrid interphase Layer on lithium metal for high-performance lithium-sulfur batteries. ACS Nano *12*, 1500–1507.
10. Li, W., Yao, H., Yan, K., Zheng, G., Liang, Z., Chiang, Y.-M., and Cui, Y. (2015). The synergetic effect of lithium polysulfide and lithium nitrate to prevent lithium denderte growth. Nat. Commun. *6*, 7436.
11. Xia, S., Zhang, X., Liang, C., Yu, Y., and Liu, w. (2020). Stabilzed lithium metal anode by an efficient coating for high-performance Li-S batteries. Energy Storage Mater. *24*, 329–335.
12. Chen, J., Yang, H., Zhang, X., Lei, J., Zhang, H., Yuan, H., Yang, J., Nuli, Y., and Wang, J. (2019). Highly reversible lithium-metal anode and lithium-sulfur batteries enabled by an intrinsic safe electrolyte. ACS Appl. Mater. Interfaces *11*, 33419–33427.
13. Yao, Y.-.X., Zhang, X.-.Q., Li, B.-.Q., Yan, C., Chen, P., Huang, J.-.Q., and Zhang, Q. (2020). A compact inorganic layer for robust anode protection lin lithium-sulfur batteries. InfoMat *2*, 379–388.
14. Pang, Q., Liang, X., Kwok, C.Y., and Nazar, L.F. (2016). Advances in lithium-sulfur batteries based on multifunctional cathodes and electrolytes. Nat. Energy *1*, 16132.
15. Gupta, A., Bhargav, A., and Manthiram, A. (2019). Highly solvating electrolytes for lithium-sulfur batteries. Adv. Energy Mater. *9*, 1803096.
16. Baek, M., Shin, H., Char, K., and Choi, J.W. (2020). Radical or Not Radical: Revisiting Lithium−Sulfur donor electrolyte for lithium-sulfur batteries. Adv. Mater.2005022
17. Barchasz, C., Molton, F., Duboc, C., Leprêtre, J.C., Patoux, S., and Alloin, F. (2012). Lithium/sulfur cell discharge mechanism: an original approach for intermediate species identification. Anal. Chem. *84*, 3973–3980.
18. Cuisinier, M., Cabelguen, P.-.E., Evers, S., He, G., Kolbeck, M., Garsuch, A., Bolin, T., Balasubramanian, M., and Nazar, L.F. (2013). Sulfur Speciation in Li−S Batteries Determined by Operando X-ray Absorption Spectroscopy. J. Phys. Chem. Lett. *4*, 3227–3232.
19. Zou, Q., Liang, Z., Du, G.-.Y., Liu, C.-Y., Li, E.Y., and Lu, Y.-.C. (2018). Cation-directed selective polysulfide stabilization in Alkali metal-sulfur batteries. J. Am. Chem. Soc. *140*, 10740–10748.
20. Chu, H., Jung, J., Noh, H., Yuk, S., Lee, J., Lee, J.-.H., Baek, J., Roh, Y., Kwon, H., Choi, D., et al. (2020). Unraveling the dual functionality of high-donor-number anion in lean-electrolyte lithium-sulfur batteries. Adv. Energy Mater. *10*, 2000493.
21. Yu, X., and Manthiram, A. (2015). A class of polysulfide catholytes for lithium-sulfur batteries: energy density cyclability and voltage enhancement. Phys. Chem. Chem. Phys. *17*, 2127–2136.
22. Elabd, A., Kim, J., Sethio, D., Kang, S., Kang, T., Choi, J.W., and Coskun, A. (2022). Dual Functional High Donor Electrolytes for Lithium−Sulfur Batteries under Lithium Nitrate Free and Lean Electrolyte Conditions. ACS Energy Lett. *7*, 2459–2468.

23. Baek, M., Shin, H., Char, K., and Choi, J.W. (2020). New high donor electrolyte for lithium-sulfur batteries. Adv. Mater. *32*, 2005022.

24. Li, G., Sun, J., Hou, W., Jiang, S., Huang, Y., and Geng, J. (2016). Three-dimensional porous carbon composites containing high sulfur nanoparticle content for high-performance lithium-sulfur batteries. Nat. Commun. *7*, 10601.

25. Chu, H., Noh, H., Kim, Y.-.J., Yuk, S., Lee, J.-.H., Lee, J., Kwack, H., Kim, Y., Yang, D.-.K., and Kim, H.-.T. (2019). Achieving three-dimensional lithium sulfide growth in lithium-sulfur batteries using high-donor-number anion. Nat. Commun. *10*, 188.

26. Fu, J., Ji, X., Chen, J., Chen, L., Fan, X., Mu, D., and Wang, C. (2020). Lithium nitrate regulated sulfone electrolytes for lithium metal batteries. Angew. Chem. Int. Ed. *59*, 22194–22201.

27. Mukra, T., Horowitz, Y., Shekhtman, I., Goor, M., Drvarič Talian, S., Burstein, L., Kasnatscheew, J., Meister, P., Grünebaum, M., Winter, M., et al. (2019). Disiloxane with nitrile and groups as co-solvent for electrolytes in lithium-sulfur batteries- afeasible approach to replace $LiNO_3$. Electrochim. Acta *307*, 76–82.

28. Shim, J., Ko, T.J., and Yoo, K. (2019). Study for an effect of $LiNO_3$ on polysulfide multistep reaction in Li/S battery. J. Ind. Eng. Chem. *80*, 283–291.

29. Li, G., Gao, Y., He, X., Huang, Q., Chen, S., Kim, S.H., and Wang, D. (2017). Organosufide-plasticized solid-electrolyte interphase layer enables stable lithium metal anodes for long-cycle lithium-sulfur batteries. Nat. Commun. *8*, 850.

30. Basile, A., Bhatt, A.I., and O' Mullane, A.P. (2016). Stabilizing lithium metal using ionic liquids for long-lived batteries. Nat. Commun. *7*, 11794.

31. Ding, F., Xu, W., Chen, X., Zhang, J., Shao, Y., Engelhard, M.H., Zhang, Y., Blake, T.A., Graff, G.L., Liu, X., and Zhang, J.-G. (2014). Effect of cesium cations in lithium deposition via self-healing electrostatic shield mechanism. J. Phys. Chem. C *118*, 4043–4049.

32. Ding, F., Xu, W., Graff, G.L., Zhang, J., Sushko, M.L., Chen, X., Shao, Y., Engelhard, M.H., Nie, Z., Xiao, J., et al. (2013). Dendrite-free Lithium deposition via self-healing electrostatic shield mechanism. J. Am. Chem. Soc. *135*, 4450–4456.

33. Dai, H., Xi, K., Liu, X., Lai, C., and Zhang, S. (2018). Cationic surfactant-based electrolyte additives for uniform lithium deposition via lithiophobic repulsion mechanisms. J. Am. Chem. Soc. *140*, 17515–17521.

34. Xiao, Y., Han, B., Zeng, Y., Chi, S.-S., Zeng, X., Zheng, Z., Xu, K., and Deng, Y. (2020). New lithium salt forms interphases suppressing both Li dendrite and polysulfide shuttling. Adv. Energy Mater. *10*, 1903937.